



# Alteration of volcanic rocks: A new non-intrusive indicator based on induced polarization measurements



A. Revil <sup>a,\*</sup>, M. Murugesu <sup>b</sup>, M. Prasad <sup>b</sup>, M. Le Breton <sup>a</sup>

<sup>a</sup> Université Grenoble Alpes, Université Savoie Mont Blanc, CNRS, IRD, IFSTTAR, ISTERRE, F-73000 Chambéry, France

<sup>b</sup> Department of Petroleum Engineering, Colorado School of Mines, Golden, CO, USA

## ARTICLE INFO

### Article history:

Received 8 February 2017

Received in revised form 13 June 2017

Accepted 19 June 2017

Available online 20 June 2017

## ABSTRACT

Induced polarization is a geophysical method investigating the ability of rocks to store reversibly electrical charges under a slowly alternating electrical field. The material property of interest is a complex-valued electrical conductivity with an in-phase component associated with conduction and a quadrature component associated with polarization. We investigated the relationship between complex conductivity spectra over the frequency range 1 mHz–45 kHz and the specific surface area (SSA) of 28 volcanic core samples extracted from a wellbore drilled for the Humu'ula Groundwater Research Project in Hawaii. The specific surface area of these samples was determined through the Brunauer, Emmett and Teller (BET) method. Subcritical nitrogen adsorption experiments were conducted using two different instruments and the samples were prepared in both pellets and powder forms. The BET specific surface area is found to be highly correlated to the cation exchange capacity of the core samples measured by the cobalthexamine method. The in-phase conductivity itself can be decomposed as the sum of a bulk contribution associated with conduction in the bulk pore water and a surface conductivity associated with conduction in the electrical double layer coating the grains. The surface conductivity, the quadrature conductivity, and the normalized chargeability (defined as the difference between the in-phase conductivity at high and low frequencies) are observed to be linearly correlated to the specific surface area or the surface per volume ratio of the core samples, which can be considered as proxy of alteration. These trends are consistent with those shown by sedimentary rocks. This new data set demonstrates that the induced polarization method can be potentially used to image alteration in volcanic environments.

© 2017 Elsevier B.V. All rights reserved.

## 1. Introduction

Flank instabilities of active and dormant volcanoes represent a significant geohazard since they may lead to edifice destabilizations with dramatic consequences for human beings. Among them, basaltic shield volcanoes, like the Hawaiian volcanoes, are the largest volcanic edifices on Earth (e.g., Moore et al., 1989; Kauahikaua et al., 2000). The action of magmatic pressure and gravitational effects leads to large scale deformation of their flanks (e.g., Iverson, 1995; Brooks et al., 2006). The geophysical monitoring of these volcanoes shows relationships between deformation, fluid flow, and mechanical stiffness (Reid, 2004; Cianetti et al., 2012). Areas of alteration constitute zones of mechanical weaknesses, changing locally the stress regime and associated induced seismicity (Urgeles et al., 1999; Masson et al., 2002; Phillips et al., 2008; Meller and Kohl, 2014). The impact of clay minerals on the mechanical properties of rocks has been broadly documented in the literature for

both sedimentary rocks (e.g., Akayuli et al., 2013) and volcanic rocks (Frolova et al., 2014). Therefore, in order to understand mechanically elastoplastic deformation on volcanoes, areas of alteration need to be imaged and monitored. Geophysical imaging techniques are expected to play an important role in that purpose (e.g., Aizawa et al., 2009a, 2009b; Siniscalchi et al., 2012).

In volcanic environments, electrical resistivity is, to some extent, sensitive to both porosity and alteration (e.g., Revil et al., 2002; Komori et al., 2010; Gonzales et al., 2014; Usui et al., 2016). Unfortunately, electrical resistivity alone is not able to image alteration because only one of its two components (called surface conductivity) is sensitive to alteration. The other component (termed bulk conductivity below) is associated with water content and salinity of the pore water. Note that both components are also sensitive to temperature with a linear dependence of approximately 2% per degree Celsius (Revil et al., 1998). Surface conductivity is associated with electrical conduction in the electrical double layer coating the surface of the grains and is therefore sensitive to the cation exchange capacity (CEC) of the material or any equivalent proxy such as the specific surface area.

Induced polarization is a geophysical technique used to characterize the reversible storage of electrical charges when a (porous) material is

\* Corresponding author.

E-mail addresses: [andre.revil@univ-smb.fr](mailto:andre.revil@univ-smb.fr) (A. Revil), [mmurugesu@mymail.mines.edu](mailto:mmurugesu@mymail.mines.edu) (M. Murugesu), [mprasad@mines.edu](mailto:mprasad@mines.edu) (M. Prasad), [mathieu.le-breton@univ-grenoble-alpes.fr](mailto:mathieu.le-breton@univ-grenoble-alpes.fr) (M. Le Breton).

submitted to a varying electrical field or electrical current at low frequencies (in the field below  $\sim 100$  Hz). The method of induced polarization was pioneered by Conrad Schlumberger (Schlumberger, 1920) for ore prospecting. This seminal work was then followed by those from Dakhnov (1941) and Bleil (1953). It was quickly discovered, however, that even in absence of metallic grains, rocks have a small but detectable low-frequency ( $< 1$  kHz) polarization (e.g., Seigel, 1959). Vacquier et al. (1957) used induced polarization to localize aquifers and aquitards. A complete theory of low frequency polarization was first developed for colloids (Lyklema et al., 1983). For sedimentary rocks, induced polarization provides a complementary approach to electrical resistivity tomography since either the quadrature conductivity or the normalized chargeability can be related to the cation exchange capacity or the specific surface area of the porous materials (e.g., Vinegar and Waxman, 1984; Börner, 1991, 1992; Weller et al., 2010).

For volcanic rocks, specific surface area measurements, using the BET nitrogen adsorption technique, can be used as a proxy of alteration (see Nielsen and Fisk, 2008). Our goal is to show that induced polarization of volcanic rocks offer a way to connect parameters (such as the quadrature conductivity and the normalized chargeability) to specific surface area measurements. This implies that induced polarization can be used to develop an attribute to image or possibly monitor alteration in volcanoes. To test such relationships, we use a set of 28 core samples extracted from a wellbore drilled for the Humu'ula Groundwater Research Project in Hawaii. In the present paper, we focus on investigating and elucidating the relationship between induced polarization parameters and specific surface area measurements of these basaltic rocks. We also compare these results with a collection of published data for sedimentary materials including soils, saprolites, sands, and sandstones for which polarization is mostly due to the presence of clay minerals.

## 2. Theory

### 2.1. Expression for the complex conductivity

An important characteristic of volcanic rocks is the existence of an electrical double layer coating the surface of their mineral grains (Fig. 1). Polarization of a porous material with silicates and aluminosilicates is due to the polarization of this electrical double layer and the adjacent pore water (Fig. 2). Schufle (1959) was probably the first to

connect induced polarization to cation exchange in the electrical double layer. Scott (2006) provided arguments in favor of such an electrical double layer polarization with a strong role played by its inner component called the Stern layer.

To simplify the presentation, we assume here that the complex conductivity of a porous material is described by a Cole-Cole model plus a dielectric effect,

$$\sigma^*(\omega) = \sigma_\infty \left[ 1 - \frac{M}{1 + (i\omega\tau_0)^c} \right] + i\omega\epsilon_\infty, \quad (1)$$

where  $\omega$  denotes the pulsation frequency,  $\epsilon_\infty$  denotes the high frequency permittivity,  $\tau_0$  is the Cole-Cole time constant,  $c$  is the Cole-Cole exponent (typically between 0 and 0.5 for sedimentary materials, see Revil et al., 2013),  $M = (\sigma_\infty - \sigma_0)/\sigma_\infty$  is the dimensionless chargeability. The normalized chargeability is defined by,

$$M_n = M\sigma_\infty = \sigma_\infty - \sigma_0, \quad (2)$$

expressed in  $S\ m^{-1}$ . The conductivities  $\sigma_0$  and  $\sigma_\infty$  denoting the DC ( $\omega = 0$ ) and high-frequency ( $\omega > 1/\tau_0$ ) electrical conductivities, respectively. The Cole Cole model will not be used explicitly in the present paper and any function characterized by a distribution of relaxation times will work as well. The high and low frequency conductivities,  $\sigma_\infty$  and  $\sigma_0$  can be obtained through a volume averaging method as underlined by Revil (2013). Note that Eq. (1) is distinct from the Cole Cole complex resistivity model also called the Pelton model (see discussion in Tarasov and Titov, 2013). The final relationships are given by

$$\sigma_0 = \frac{1}{F} \sigma_w + \left( \frac{1}{F\phi} \right) \rho_g \beta_{(+)} (1-f) CEC, \quad (3)$$

$$\sigma_\infty = \frac{1}{F} \sigma_w + \left( \frac{1}{F\phi} \right) \rho_g [\beta_{(+)} (1-f) + \beta_{(+)}^S f] CEC, \quad (4)$$

where  $\sigma_w$  (in  $S\ m^{-1}$ ) denotes the pore water conductivity,  $F$  (dimensionless) the intrinsic formation factor related to the connected porosity  $\phi$  by Archie's law  $F = \phi^{-m}$  with  $m \geq 1$  being the cementation or porosity exponent (Archie, 1942),  $f$  (dimensionless) denotes the partition coefficient (fraction of counterions in the Stern layer),  $\rho_g$  is the grain density (in  $kg\ m^{-3}$ , typically  $\rho_g = 2650\ kg\ m^{-3}$  for sedimentary rocks and 3000

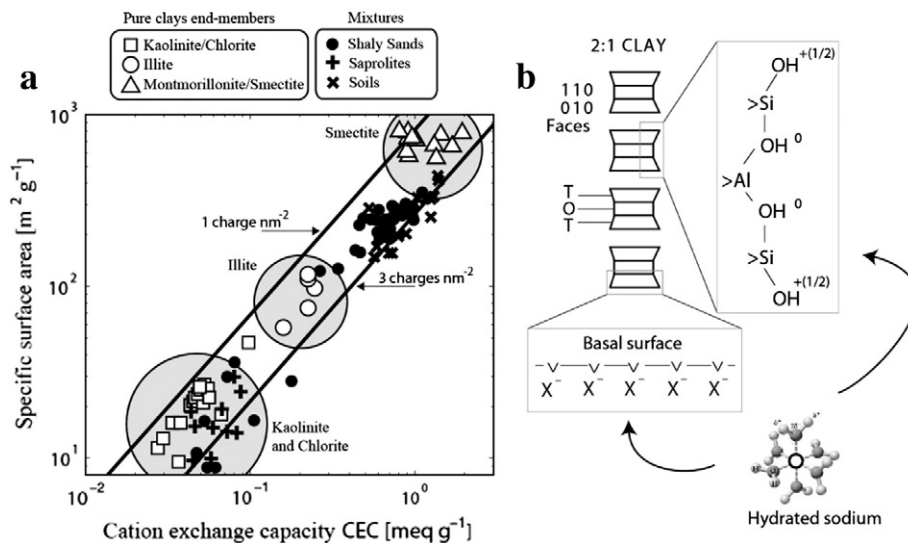


**Fig. 1.** Relationship between specific surface area (SSA) and cation exchange capacity (CEC) for clay minerals and clay-rich porous materials. a. Specific surface area as a function of CEC (in  $meq\ g^{-1}$  with  $1\ meq\ g^{-1} = 96,320\ C\ kg^{-1}$  in SI units). The two lines correspond to 1 to 3 elementary charges per unit surface area. Modified from Revil et al. (2013). The data shows therefore that the average surface charge density is around 2 elementary charges per  $nm^2$  ( $Q_s = 0.32\ C\ m^{-2}$ ). b. Sodium is weakly sorbed on the basal surface of the clay minerals (in the diffuse layer) and more strongly on the edges of the clay crystals (mostly in the diffuse layer). The partition coefficient (dimensionless)  $f$  defines the relative amount of cations (counterions) sorbed in the Stern layer with respect to the total amount of counterions sorbed in the diffuse and Stern layers.

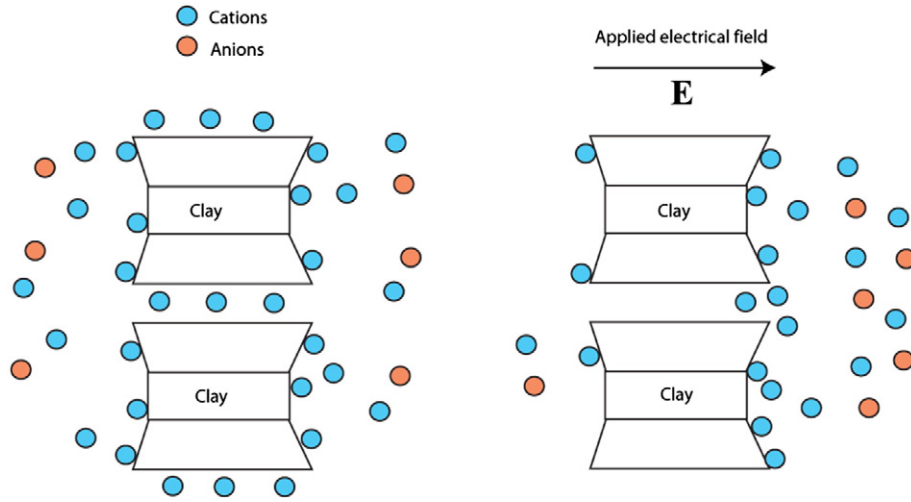


**Fig. 2.** Sketch of the polarization of a clay grain in a volcanic rock. In equilibrium, there is an excess of cations (in blue) associated with the clay grains both in the diffuse layer associated with the basal planes and the amphoteric sites covering the edges of the clay crystal and the Stern layer on the edges. In presence of an electrical field  $E$ , the clay particles get polarized due to the electromigration of the cations in the direction of the electrical field (Stern layer polarization) and the formation of a salinity gradient on each side of the grain (membrane polarization). This polarization provides a dipole moment to the clay particles. Note that the migration of the charge carriers is, in both cases, controlled by electrochemical potential gradients, so, fundamentally, there is no difference in the physics involved in both Stern layer and membrane polarization mechanisms.

$\pm 200 \text{ kg m}^{-3}$  for volcanic rocks), and CEC is the cation exchange capacity (in  $\text{C kg}^{-1}$ ). Note that the CEC can be expressed in different units such as  $\text{meq}/100 \text{ g}$  or  $\text{mol}/\text{kg}$  (i.e., a concentration of sorbed species such as cobalt over the mass of dry grains (and  $1 \text{ meq g}^{-1} = 1 \text{ mol}/\text{kg} = 96,320 \text{ C kg}^{-1}$ ). In the present case, we convert the CEC into a charge per mass of grains using the Faraday number corresponding to the product of the Avogadro number ( $N = 6.02 \times 10^{23} \text{ mol}^{-1}$ ) and the value of the elementary charge ( $e = 1.6 \times 10^{-19} \text{ C}$ , where C stands for Coulomb). The Faraday number ( $96,320 \text{ C mol}^{-1}$ ) denotes the absolute value of the charge of a mole of electrons.

The values of the mobility of ions in diffuse layer are the same than in the bulk pore water (Revil, 2012). For sodium, we have  $\beta_{(+)}(\text{Na}^+, 25^\circ \text{C}) = 5.2 \times 10^{-8} \text{ m}^2 \text{ s}^{-1} \text{ V}^{-1}$ . The reason is that the viscosity in the diffuse layer is the same than in the bulk pore water so the mobility of the ions remains the same. Things may be different in the inner part of the electrical double layer called the Stern layer. This will be discussed in the last part of this paper.

The characteristic relaxation time entering Eq. (1),  $\tau_0$ , is associated with a characteristic pore size  $\Lambda$  (eventually a grain size) according to  $\tau_0 = \Lambda^2 / 2D_{(+)}^S$ , where  $D_{(+)}^S$  denotes the diffusion coefficient of the counterions in the Stern layer (expressed in  $\text{m}^2 \text{ s}^{-1}$ ). The value of this diffusion coefficient  $D_{(+)}^S$  should be related to the mobility of the counterions in the Stern layer,  $\beta_{(+)}^S$ , by the Nernst-Einstein relationship  $D_{(+)}^S = k_b T \beta_{(+)}^S / |q_{(+)}|$ , where  $T$  denotes the absolute temperature (in K),  $k_b$  denotes the Boltzmann constant ( $1.3806 \times 10^{-23} \text{ m}^2 \text{ kg s}^{-2} \text{ K}^{-1}$ ),  $|q_{(+)}|$  is the charge of the counterions in the Stern layer coating the surface of the grains ( $|q_{(+)}| = e$  for  $\text{Na}^+$  and where  $e$  is the elementary charge expressed in C).

Eqs. (3) and (4) can be written as

$$\sigma' = \frac{1}{F} \sigma_w + \sigma_S \tag{5}$$

where the first term of Eq. (5) refers to the bulk conductivity in the connected pore space and where  $\sigma_S$  (in  $\text{S m}^{-1}$ ) denotes the surface conductivity of the material, i.e., the conductivity associated with the influence of the electrical double layer. At high frequencies, the surface conductivity and the normalized chargeability are expressed by (Revil, 2013)

$$\sigma_S = \left( \frac{1}{F\phi} \right) \rho_g \left[ \beta_{(+)}(1-f) + \beta_{(+)}^S f \right] \text{CEC}, \tag{6}$$

$$M_n = \left( \frac{1}{F\phi} \right) \rho_g \beta_{(+)}^S f \text{CEC}. \tag{7}$$

According to Eq. (7), the normalized chargeability depends on the properties of the grains ( $\rho_g$  and CEC), the properties of the Stern layer ( $\beta_{(+)}^S$  and  $f$ ), and the texture of the volcanic rock through its dependence with the bulk tortuosity  $F\phi$ .

### 2.2. Relationship to specific surface area

The charge density per unit surface area,  $Q_S$  (in  $\text{C m}^{-2}$ ), denotes the available charge density of counterions that can be sorbed on the mineral surface in both the diffuse and Stern layers. It is therefore defined as the ratio of the CEC by the specific surface area of the material  $S_{Sp}$  (in  $\text{m}^2 \text{ kg}^{-1}$ )

$$Q_S = \frac{\text{CEC}}{S_{Sp}}. \tag{8}$$

The specific surface area can be measured by the so-called BET technique using nitrogen adsorption (see details in Lowell and Shields, 1979). For clay minerals, the mean charge density  $Q_S$  is typically 2 elementary charges per  $\text{nm}^2$  ( $Q_S = 0.32 \text{ C m}^{-2}$ ) (see Fig. 1). As shown in Fig. 1, this charge is an average of the charge related to the isomorphous substitutions and the charge associated with the amphoteric sites on the edge of the clay crystals. From Eqs. (6) to (8), the surface conductivity and the normalized chargeability depend on the specific surface area according to,

$$\sigma_S = \left( \frac{1}{F\phi} \right) \rho_g \left[ \beta_{(+)}(1-f) + \beta_{(+)}^S f \right] Q_S S_{Sp}, \tag{9}$$

$$M_n = \left( \frac{1}{F\phi} \right) \rho_g \beta_{(+)}^S f Q_S S_{Sp}, \tag{10}$$

respectively. These equations show that the surface conductivity and the normalized chargeability (therefore the quadrature conductivity) are also controlled by the tortuosity of the bulk pore space  $F\phi$  (Revil, 2013). The dependence of the surface conductivity and quadrature conductivity with the tortuosity of the bulk pore space was demonstrated

recently by Revil et al. (2014) for a collection of Fontainebleau sandstones. For the Fontainebleau sandstones, all the terms entering Eqs. (9) and (10) are constant with the exception of the bulk tortuosity (see Revil et al., 2014 for details). This makes this rock perfect to test the sensitivity of the surface conductivity to this parameter.

### 2.3. Relationship to surface per pore volume ratio

Two other quantities of interest are the charge per unit pore volume (used instead of the CEC, i.e., the charge per unit mass of grains) and the surface per pore volume ratio (used instead of the specific surface area, i.e., a surface per unit mass of grains). These parameters are defined by,

$$Q_V = \rho_g \left( \frac{1-\phi}{\phi} \right) \text{CEC}, \quad (11)$$

$$S_{por} = \frac{S}{V_p} = \rho_g \left( \frac{1-\phi}{\phi} \right) S_{sp}, \quad (12)$$

respectively. The inverse of this quantity grossly corresponds to a hydraulic radius (for a capillary, it would be exactly the radius of the capillary). As shown by Revil (2013), these parameters can be used to determine the surface conductivity and normalized chargeability (hence the quadrature conductivity at the frequency peak). This yields,

$$\sigma_S = \frac{1}{F} B Q_V. \quad (13)$$

$$M_n = \frac{1}{F} \lambda Q_V. \quad (14)$$

with  $B = \beta_{(+)}(1-f) + \beta_{(+)}^S f$  being an apparent mobility for surface conduction (and similarly  $\lambda = \beta_{(+)}^S f$  for the quadrature conductivity). The equivalent linear circuit of a volcanic rock can be sketched as in Fig. 3 and can be seen as two resistances in parallel to a capacitance.

Since the surface charge density is related to the volumetric charge density by  $Q_S = Q_V V_p / S$ , we have,

$$\sigma_S = \frac{1}{F} B Q_S S_{por}. \quad (15)$$

$$M_n = \frac{1}{F} \lambda Q_S S_{por}. \quad (16)$$

(and similarly for the quadrature conductivity). Eq. (15) is similar to the equations developed empirically by Waxman and Smits (1968) and Cremers (1968). An equation similar to Eq. (16) for the quadrature conductivity can also be found in Vinegar and Waxman (1984). Eqs. (15) and (16) are also similar to the equations developed by Börner (1991, 1992) for the surface conductivity and the quadrature conductivity. According to Revil (2013), these Eqs. (13) to (16) are however only valid for high porosity rocks. They are not derived directly from Eqs. (9) and (11) (there is a discrepancy by a factor  $(1-\phi)$  between these equations, see discussions in Revil, 2013).

### 2.4. The quadrature conductivity

We conclude this section with the following remarks. The surface conductivity and the normalized chargeability can be difficult to accurately determine. The surface conductivity is difficult to determine because the linear conductivity model described above is only valid when the surface conductivity is small with respect to the bulk conductivity (high salinity assumption, see discussion in Bernabé and Revil, 1995). When surface conductivity is dominant, this high salinity linear assumption used above is not valid anymore. The relationship between the conductivity of the porous material and the pore water conductivity becomes non-linear (e.g., Revil et al., 1998). This non-linearity is reflected in the Waxman and Smits (1968) model by having an

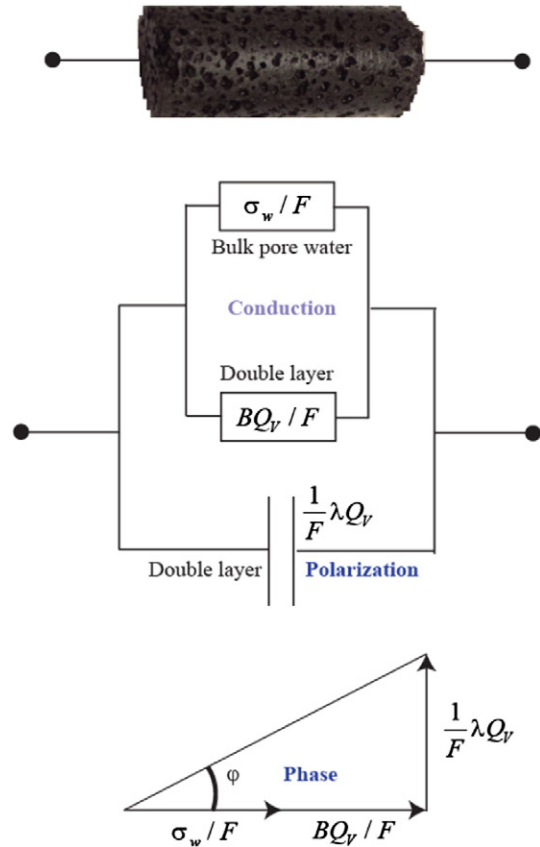


**Fig. 3.** First order approximation of the equivalent circuit of a volcanic rock (Maxwell Wagner polarization excluded). Conduction comprises two contributions, one associated with the bulk pore water ( $\sigma_w/F$  where  $\sigma_w$  denotes the pore water conductivity and  $F$  the formation factor) and the other with conduction in the electrical double layer (surface conductivity  $BQ_V/F$  where  $B$  is an equivalent mobility for the counterions and  $Q_V$  an excess charge of counterions per unit pore volume). The capacitance corresponds to the polarization of the electrical double layer coating the surface of the grains and  $\lambda$  denotes an equivalent mobility for the counterions for the quadrature conductivity. The tangent of the phase angle  $\varphi$  represents the ratio between polarization and conduction (modified from Vinegar and Waxman, 1984).

apparent mobility  $B$  that decrease with salinity at low salinities. The normalized chargeability may also be difficult to accurately measure since it requires very broadband measurements (typically over 7 decades). In time domain induced polarization, the normalized chargeability can be measured but requires that all the polarization length scales have been fully polarized, which can be only achieved through a long duration (>100 to 200 s) of the primary current injection. The quadrature conductivity is easily measurable but its value is frequency dependent. In addition at high frequencies, > 1 kHz, the quadrature conductivity associated with the polarization of the double layer of the grains can be masked by the Maxwell Wagner polarization. Following Revil et al. (2015), we can define a linear relationship between the quadrature conductivity and the normalized chargeability,

$$\sigma'' \approx -\frac{M_n}{\alpha}, \quad (17)$$

where  $\alpha$  has been taken equal to 1 or 5 in Revil et al. (2015). The value of  $\alpha$  will be determined below. Following Revil et al. (2015), we use the following definition for the dimensionless number  $R$ :

$$R \equiv \frac{M_n}{\sigma_S} \approx -\alpha \left( \frac{\sigma''}{\sigma_S} \right), \quad (18)$$

and  $-\sigma''/\sigma_s = R/\alpha$ . Using Eqs. (6) and (7), or alternatively Eqs. (15) and (16), this dimensionless number  $R$  can be related to the partition coefficient  $f$  (e.g., Revil et al., 2015) by

$$R = \frac{\beta_{(+)}^S f}{[\beta_{(+)}(1-f) + \beta_{(+)}^S f]} \quad (19)$$

We will use the ratio between quadrature conductivity and surface conductivity to determine the value of  $R$  in Section 5 below.

### 3. Experiments

#### 3.1. Complex conductivity measurements

We use a four electrodes technique to do the complex conductivity measurements, i.e., we separate the current electrodes A and B from the voltage electrodes M and N. The voltage electrodes are Ag–AgCl electrodes. The current electrodes are stainless steel plates with the same diameter as the core sample. The sample is located inside an elastic and insulating jacket to avoid the drying of the core sample during the measurements. The complex conductivity measurement was conducted with a high-precision impedance analyzer (Zimmermann et al., 2008). The measured resistances were transformed in resistivity using a geometrical factor numerically computed based on the geometry of the sample and the position and size of the electrodes.

The core samples were initially saturated with a low salinity NaCl solution in a vacuum chamber for 24 h. Then samples were left a week in the solution in a closed container, and fluid conductivity was measured, until reaching stability. Afterwards, the samples were taken out for complex conductivity measurement under frequency from 1 MHz to 45 kHz. Complex conductivity spectra of the core samples were obtained at various pore fluid conductivities (0.07, 0.5, 1.0 or 2 S m<sup>-1</sup>, and 10 S m<sup>-1</sup>).

#### 3.2. Other measurements

The properties of the 28 core samples are listed in Table 1. The CEC measurements were obtained using cobalt hexamine chloride method. The porosity and density of the grains were determined using the volume and mass of the dry and saturated core samples.

Subcritical nitrogen adsorption has the ability to cover a wide range of pore sizes, from micro- to meso- to macro-pores (as defined by the IUPAC). The specific surface area experiments were conducted using two different instruments, namely the Micromeritics ASAP 2020™ and the Quadrasorb EVO/SI (Fig. 4). The core samples were prepared in both pellet and in powder form. We used one to three grams of sample in the Micromeritics ASAP 2020™ and slightly larger amounts in the Quadrasorb EVO/SI, in order to obtain accurate isotherms above the noise level. The samples were degassed at 200 °C for a minimum of 12 h under a vacuum condition of <0.005 Torr/min (Kuila, 2007). Degassing ensures complete removal of physically adsorbed unwanted vapours and gases from the sample's internal and external surface (Thommes and Cychosz, 2014). Before degassing, weight of the empty sample tube was measured three times. Then, the tube with sample was weighed three times. After degassing, the tube with degassed sample was weighed three times again.

After degassing, the tube with evacuated samples was analyzed using liquid Nitrogen at 77 K. Void space of the sample cell was measured using Helium gas (Kuila, 2007). A dewar filled with liquid nitrogen completely surrounds the sample to keep the temperature surrounding the sample at 77 K. As a given relative pressure is reached, some nitrogen sorbs on the sample. Relative pressure ( $P/P_0$ ) is defined as the current pressure  $P$  divided by the saturation vapour pressure of Nitrogen  $P_0$ . The relative pressure ranges from 0.03 to 0.995 at a constant temperature. During adsorption, the relative pressure is

**Table 1**

Relevant petrophysical of the 28 core samples (label HG denotes the HGRP project discussed in more details in the first paper of this series) used in the present manuscript. The parameter  $\phi$  denotes the connected porosity (dimensionless),  $\rho_g$  the grain density (kg m<sup>-3</sup>),  $F$  the electrical (intrinsic) formation factor (dimensionless), CEC (meq/100 g) denotes the cation exchange capacity, and  $S_{sp}$  denotes the specific surface area measured with the BET method.

Sample	$\phi$ (-)	$\rho_g$ (kg m <sup>-3</sup> )	$F$ (-)	CEC (meq/100 g)	$S_{sp}$ (m <sup>2</sup> g <sup>-1</sup> )	$\sigma_s$ (10 <sup>-4</sup> S m <sup>-1</sup> )
HG7	0.114	2880	172	0.483	0.64	4.5
HG44	0.065	2850	158	0.199	0.20	3.1
HG78	0.204	3010	44	0.256	0.25	13.7
HG137	0.064	2990	305	0.199	0.49	5.9
HG157	0.146	3050	176	0.482	1.04	4.0
HG179	0.189	2080	56	0.312	0.63	4.5
HG279	0.103	3040	240	0.398	0.77	5.7
HG341	0.198	2720	114	0.625	1.52	4.4
HG365	0.080	2450	132	0.397	0.64	3.3
HG444	0.131	2970	167	0.663	0.80	5.9
HG463	0.129	3070	143	0.738	0.83	14.4
HG482	0.323	3070	33	0.454	-	5.9
HG524	0.328	3070	29	0.653	1.20	9.4
HG552	0.185	2940	112	0.426	0.93	14.2
HG554	0.117	2840	208	0.750	0.87	10.7
HG583	0.178	2820	108	5.37	3.20	7.7
HG623	0.323	3350	31	1.31	2.40	47.4
HG723	0.292	3220	42	0.45	0.70	7.7
HG761	0.297	3000	29	2.07	0.86	43.2
HG785	0.134	3020	80	0.43	0.65	4.1
HG804	0.311	3060	37	1.68	4.43	13.7
HG820	0.184	3010	58	5.05	5.75	34.1
HG851	0.153	3000	148	4.99	6.63	36.9
HG904	0.077	3010	139	11.36	6.72	115
HG919	0.255	3030	50	11.27	7.35	172
HG921	0.308	2840	32	7.52	4.61	230
HG924	0.261	3100	82	22.68	13.29	221
HG1058	0.149	3360	40	23.93	7.86	795

systematically increased while recording the volume of N<sub>2</sub> adsorbed (cm<sup>3</sup>/g) at each partial pressure. During desorption, the relative pressure is dropped from the saturation pressure to almost  $P/P_0 = 0.05$ . The underlying theory of the BET approach can be found in Brunauer et al. (1938) and is used to determine the specific surface area of the core samples.

## 4. Results

#### 4.1. Specific surface areas

The graphs below show the 28 isotherm results obtained. From Fig. 4, it becomes apparent that both instruments produce similar patterns of isotherms for the samples. Thus, for this paper, we will not differentiate the results by instrument. The specific surface areas are reported in Table 1.

Note that nitrogen adsorption only measures the external specific surface area. Recently, Thommes and Cychosz (2014) have shown that nitrogen is not optimal for determining the micropore size distributions due to its quadrupole moment. Possibly, our measured total specific surface areas (TSSA) are lower than if a gas such as Argon would have been used. This underestimation of TSSA by the nitrogen adsorption method might lead to an overestimation of the charge density. The values of the pore volume ratio are also determined in Table 2 from the porosity and the specific surface area measurements.

#### 4.2. Surface charge density

The material properties used in the present study are summarized in Tables 1 and 2. In Fig. 5, we plot the specific surface area data versus the cation exchange capacity for the volcanic rocks investigated in the

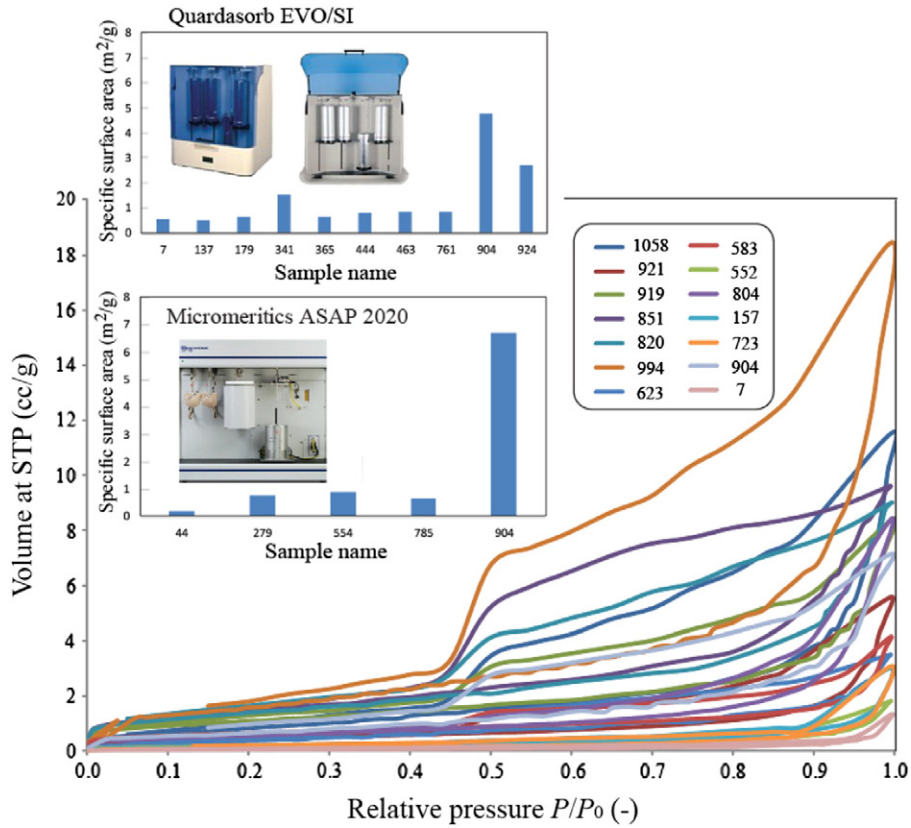


Fig. 4. BET sorption and desorption curves. Nitrogen sorption isotherms measured with two distinct instruments. Several samples (for instance Sample #904) were measured with the two methods described in the main text and the resulting values of the specific surface area are consistent.

Table 2

Relevant petrophysical of the 28 core samples (label HG denotes the HGRP project discussed in more details in the first paper of this series) used in the present manuscript.  $k$  ( $m^2$ ) denotes the measured air permeability (in mD with  $1 \text{ mD} \approx 10^{-15} \text{ m}^2$ ) corrected for the Klinkenberg effect,  $\sigma'$  denotes the absolute value of the quadrature conductivity at  $\alpha_w = 0.07 \text{ S m}^{-1}$  and 1 kHz. The ratio  $V_p/S$  can be seen as a rough estimate of the pore radius for the microporosity associated with the alteration.

Sample	$k$ (mD)	$\sigma'$ ( $10^{-5} \text{ S m}^{-1}$ )	$V_p/S$ ( $\mu\text{m}$ )	$M_n$ ( $\text{S m}^{-1}$ )
HG7	0.195	4.60	0.067	0.0009
HG44	0.314	3.91	0.116	0.00025
HG78	-	16.5	0.342	-
HG137	-	6.11	0.047	-
HG157	2.201	9.07	0.055	0.00077
HG179	0.478	9.27	0.123	0.00085
HG279	1.596	8.19	0.050	0.0013
HG341	6.17	10.2	0.054	0.0014
HG365	-	6.54	0.045	-
HG444	2.134	5.78	0.063	0.00065
HG463	0.07	11.1	0.059	0.0032
HG482	0.239	18.1	-	0.0015
HG524	0.02	27.4	0.136	0.0022
HG552	3.586	5.71	0.081	0.0008
HG554	0.018	8.45	0.051	0.0012
HG583	7.87	-	0.023	0.0007
HG623	-	17.1	0.066	-
HG723	98.14	23.1	0.196	0.002
HG761	-	12.8	0.164	-
HG785	112.9	7.83	0.079	0.0007
HG804	-	15.5	0.034	-
HG820	0.172	32.7	0.013	-
HG851	0.004	18.1	0.009	-
HG904	0.058	54.3	0.004	0.017
HG919	0.007	64.8	0.016	0.15
HG921	0.002	22.5	0.032	0.0045
HG924	0.002	95.0	0.009	0.0547
HG1058	0.001	184	0.007	-

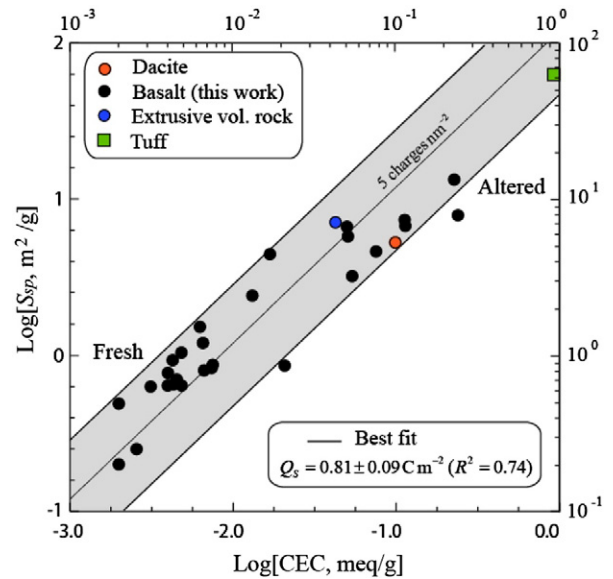
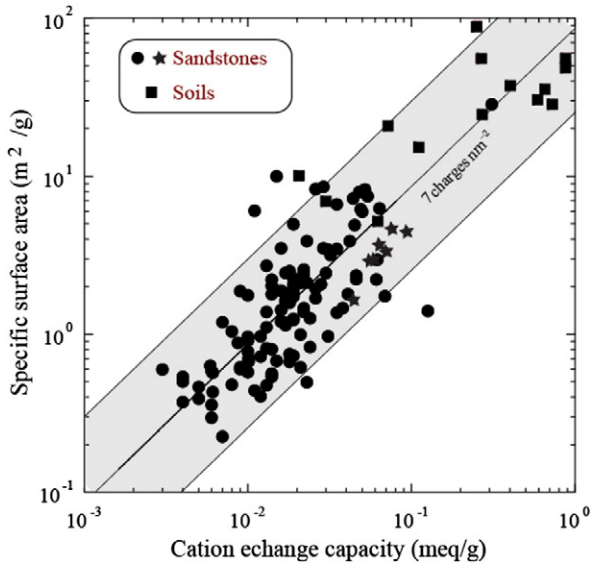


Fig. 5. Specific surface area (SSA) versus Cation exchange capacity (CEC) for the volcanic rocks ( $1 \text{ meq} = 96.32 \text{ C}$ ). The linear trend (in a log log plot) is used to determine the average surface charge density of the mineral surface, which is  $-5$  elementary charges per  $\text{nm}^2$  ( $Q_s = 0.81 \pm 0.08 \text{ C m}^{-2}$ ). The dacite data ( $\text{CEC} = 0.10 \text{ meq g}^{-1}$ ,  $\text{SSA} 6.4 \text{ m}^2 \text{ g}^{-1}$ ) are from Shinzato et al. (2012, CEC obtained with the  $\text{NH}_4\text{-Na}$  titration method). The data for the extrusive volcanic rock ( $\text{CEC} = 0.0404 \text{ meq g}^{-1}$ ,  $\text{SSA} 7.0 \text{ m}^2 \text{ g}^{-1}$ ) are from Lira et al. (2013, CEC measured with the ammonium acetate method and SSA with the BET method). The tuff data ( $\text{CEC} = 0.98 \text{ meq g}^{-1}$ ,  $\text{SSA} 63.0 \text{ m}^2 \text{ g}^{-1}$ ) are from Godelitsas et al. (2010). Note the increase of the surface charge density with the alteration.



**Fig. 6.** Cation exchange capacity versus specific surface area for sedimentary rocks and soils (1 meq = 96.32 C). The trend is used to determine the surface charge density, which is around 7 elementary charges per nm<sup>2</sup> ( $Q_s = 1.12 \pm 0.12 \text{ C m}^{-2}$ ). The sandstone data are from Sen et al. (1990). For the sandstones, the CEC was measured with the ammonium (NH<sub>4</sub>) titration method described in details by Ridge (1983). Specific surface areas were all measured with the BET technique using nitrogen sorption (Lowell and Shields, 1979). For the soils, the CEC was determined with the NH<sub>4</sub>-Na method (by titration) and the specific surface area was obtained with the BET nitrogen sorption method (data from Yukselen and Kaya, 2008). The stars correspond to the data from Mejus (2014) (St Bees sandstones).

present study in addition to few rocks from the literature. The two quantities are proportional to each other with an average surface charge density (ratio of the CEC to the specific surface area) equivalent to 5 elementary charges per nm<sup>2</sup>. This value is consistent with what is found in sedimentary rocks (see Fig. 6).

4.3. Normalized chargeability versus quadrature conductivity

An example of complex conductivity spectrum for sample #44 is shown in Fig. 7. Our goal here is to establish a new relationship between

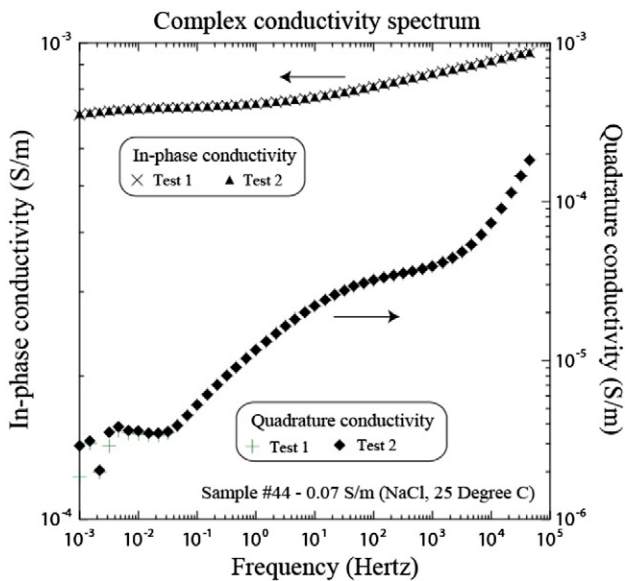


**Fig. 7.** Complex electrical conductivity spectrum for a volcanic core sample at low pore water electrical conductivity. The acquisition of the spectra has been repeated twice showing the very high repeatability of the measurements.

the normalized chargeability and the quadrature conductivity. Such relationship is important to connect induced polarization usually performed in field conditions in time-domain (and measuring the chargeability) to frequency-domain induced polarization data such as presented in this paper. The frequency effect FE can be determined from the variation with the frequency of in-phase conductivity according to:

$$FE = \frac{\sigma'(A\omega) - \sigma'(\omega)}{\sigma'(A\omega)}, \tag{20}$$

and therefore characterizes the change in in-phase conductivity between two angular frequencies  $\omega$  and  $A\omega$ . This frequency effect can be related to the phase angle  $\varphi$  measured at the geometric frequency  $A^{1/2}\omega$  by (Shuey and Johnson, 1973, and Van Voorhis et al., 1973)

$$FE \approx -\frac{2}{\pi} \varphi \ln A, \text{ for } \varphi \ll 1. \tag{21}$$

Eq. (21) was derived using two distinct complex conductivity models that are different from the Cole Cole model corresponding to Eq. (1). However, when the value of the c-exponent is small, i.e., there is a broad distribution of relaxation times, the quadrature conductivity spectra are rather flat and therefore quite similar to the constant phase model (Drake's model) used for instance by Van Voorhis et al. (1973).

Coming back to our data set, we chose to check the validity of Eq. (21) over one decade (i.e.,  $A = 10$ ) between 1 Hz and 10 Hz. In this case, according to Eq. (21) the percentage frequency effect (PFE) is given by  $PFE = 100FE \approx 0.1467 \varphi$  (Vinegar and Waxman, 1984) where the phase is here expressed in mrad. In Fig. 8, we use all of the sample data to study if this relationship is obeyed for in phase conductivity measured between 1 and 10 Hz and the phase measured at the geometric mean (3.2 Hz).

Pushing our analysis one step further, Eqs. (20) and (21) can be used to determine a relationship between the quadrature conductivity and the normalized chargeability. We assume that the conductivity itself is not a strong function of the frequency (as mentioned above) and which is the case for porous rocks (see the magnitude of the PFE in

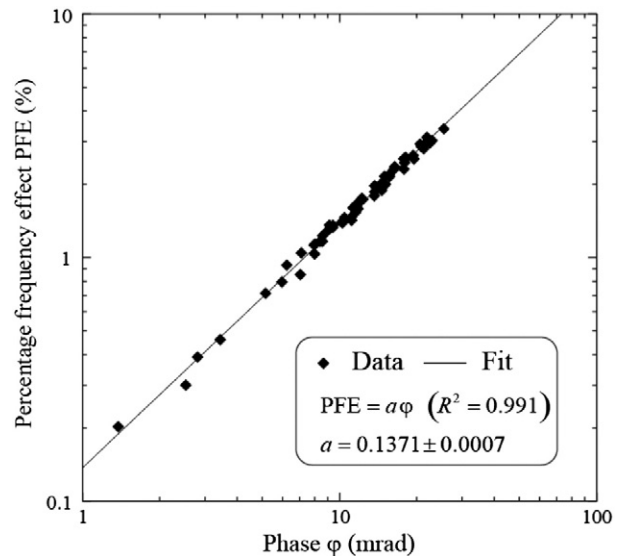


**Fig. 8.** Consistency test for the complex conductivity spectra for the three lowest salinities. The percentage frequency effect PFE is determined from the change of the real (in-phase) conductivity data between 1 Hz and 10 Hz (1 decade change). The PFE is compared with the phase lag measured at 3.2 Hz, i.e., at the geometric value of the frequency between 1 Hz and 10 Hz. This test shows that our dataset follows the prediction of the Drake's model.

Fig. 8). Then, we consider that the quadrature conductivity is determined close to the peak frequency used as the geometric mean frequency between a low frequency for which the conductivity is close to  $\sigma_0$  and a high frequency for which the conductivity is close to  $\sigma_\infty$ . In this case, Eq. (21) can be written as an equation for the normalized chargeability and the quadrature conductivity,

$$M_n \approx -\left(\frac{2}{\pi} \ln A\right) \sigma'' \tag{22}$$

where  $\log(A)$  denotes the number of decades separating high and low frequencies. Eq. (22) provides a direct way to estimate the value of  $\alpha$  in Eq. (17). Comparing the two equations, we have indeed,

$$\alpha \approx -\left(\frac{2}{\pi} \ln A\right) \tag{23}$$

If we assume that high and low frequencies are separated by 6 decades ( $A = 10^6$ ), we obtain  $\alpha \approx 8.8$  while if we use 7 decades, we obtain  $\alpha \approx 10.3$ . We will consider therefore  $\alpha \approx 10$  in the following calculations. It is therefore remarkable that the proportionality between the normalized chargeability and the quadrature conductivity is pretty well constrained. We will see later, in Section 4.4, that this value is consistent with a broad range of experimental data.

In order to test Eq. (23), we perform an additional test on our data using all the core samples. We compare in Fig. 9, the normalized chargeability between 1 Hz and 1 kHz and the quadrature conductivity determined at the geometric mean frequency of 32 Hz. This normalized chargeability is defined as the difference in the in-phase conductivity between 1 kHz and 1 Hz. The data shown in Fig. 9 exhibit a very high linear trend with a slope  $\alpha = 4.88 \pm 0.02$ . Eq. (23) predicts a slope of 4.40, therefore close enough. In Fig. 10, we compare the normalized chargeability now determined over the frequency range 0.1 Hz–10 kHz (so 5 decades,  $A = 10^5$ ) with the quadrature conductivity at the geometric mean frequency of 32 Hz. The data shown in Fig. 10 exhibit a linear trend with a slope  $\alpha = 10.2 \pm 0.2$ . Eq. (23) predicts a slope of 7.3, so a bit below the slope shown by the data.

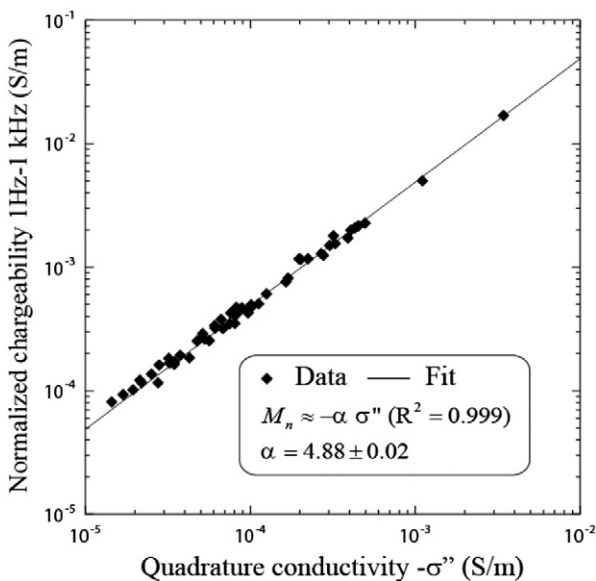


Fig. 9. Relationship between the normalized chargeability (determined from the variation of the in-phase conductivity between 1 Hz and 1 kHz, i.e., over three decades) and the quadrature conductivity (at the geometric mean frequency of 32 Hz) for the volcanic rocks.

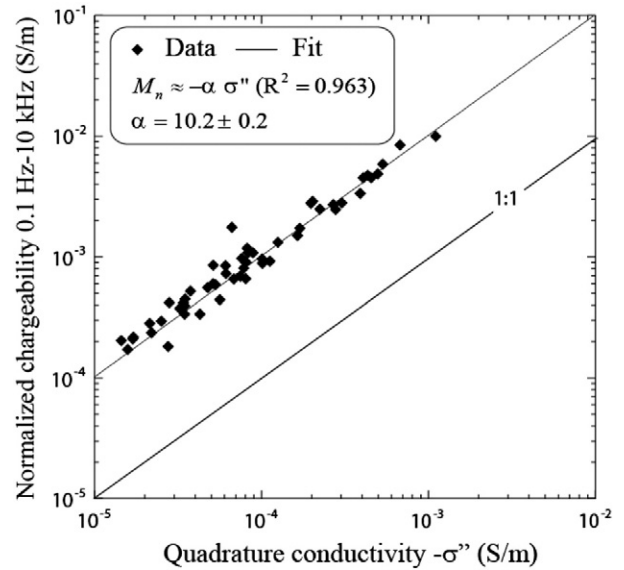


Fig. 10. Relationship between the normalized chargeability (determined from the variation of the in-phase conductivity between 0.1 Hz and 10 kHz, i.e., over 5 decades) and the quadrature conductivity (at the geometric mean frequency of 32 Hz) for the volcanic rocks. We see that the normalized chargeability is approximately 10 times higher than the quadrature conductivity for a normalized chargeability estimated over 5 decades.

#### 4.4. Surface conductivity

In order to determine the intrinsic formation factor and the surface conductivity of the various core samples (reported in Table 1), we use the in-phase conductivity data measured at different pore water conductivities. We fit these data, at different frequencies, with Eq. (5) (see Fig. 11 for core sample #924). The surface conductivity data are then normalized with respect to the tortuosity and plotted as a function of the specific surface area in Fig. 12. We see that the data are linearly correlated as predicted by Eq. (9). We obtain  $a = \rho_g [\beta_{(+)}(1-f) + \beta_{(+)}^s f] Q_s = 1.6 \times 10^{-5} \text{ kg C m}^{-3} \text{ V}^{-1} \text{ s}^{-1}$

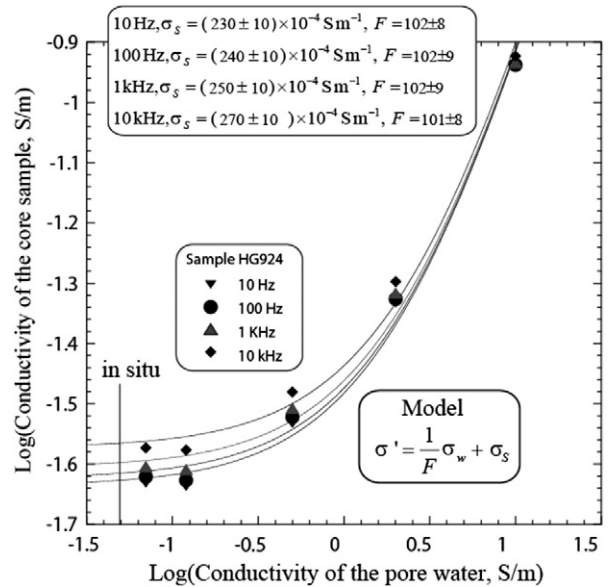
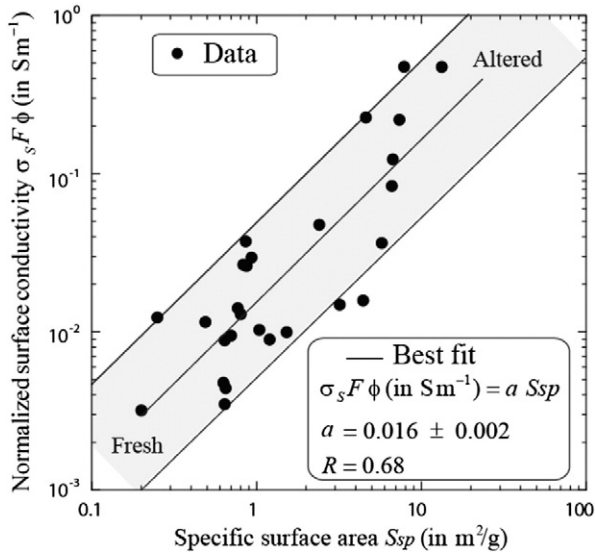


Fig. 11. Conductivity of the rock versus the conductivity of the pore water (NaCl brine, 25 °C) for a volcanic core sample (Sample HG924). The linear equation between the two quantities is fitted with the model displayed in the figure in order to get the value of the intrinsic formation factor  $F$  and the surface conductivity  $\sigma_s$ . “in situ” corresponds to the pore water conductivity of the connate water at the place where the core sample was extracted.



**Fig. 12.** Relationship between the normalized surface conductivity and the specific surface area (expressed here in  $\text{m}^2 \text{g}^{-1}$ ) measured with the BET method for the volcanic rock samples investigated in the present study. The normalized surface conductivity is obtained by multiplying the surface conductivity (defined by Eq. (5)) with the tortuosity (product of the intrinsic formation factor with the connected porosity). Both the surface conductivity and the formation factor are determined by the type of plot shown in Fig. 11.

or if we use  $B = \beta_{(+)}(1-f) + \beta_{(+)}^S f$ , this yields  $B = 4.3 \times 10^{-9} \text{ m}^2 \text{ V}^{-1} \text{ s}^{-1}$  where we have used  $\rho_g = 3000 \text{ kg m}^{-3}$  (Table 1) and  $Q_S = 0.81 \text{ C m}^{-2}$  (Fig. 5).

In Fig. 13, we compare the surface conductivity versus specific surface area trend data obtained with the volcanic rocks with the trend shown by the literature data for sedimentary rocks and some clay materials. The results are consistent, indicating that the same relationship can be used for sedimentary and volcanic rocks.

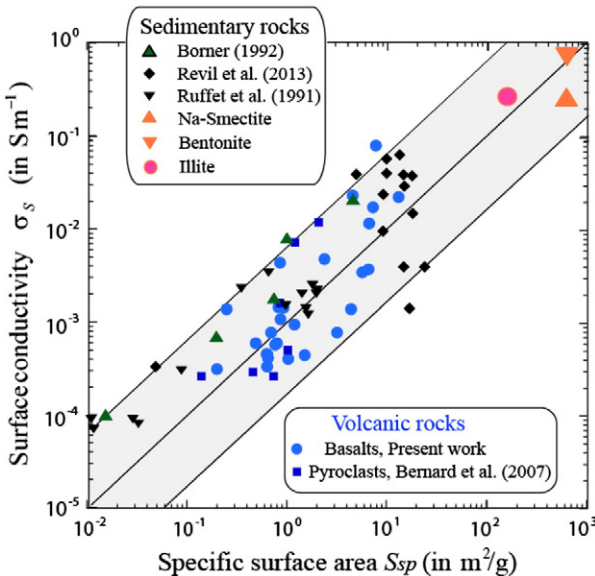


**Fig. 13.** Relationship between the surface conductivity and the specific surface area (expressed here in  $\text{m}^2 \text{g}^{-1}$  and measured with the BET method) for volcanic and sedimentary rocks (no carbonates). Experimental data from Bernard et al. (2007), Börner (1992), Revil et al. (2013), and Ruffet et al. (1991). For the smectite (Na-Montmorillonite), the specific surface area is  $700 \text{ m}^2 \text{g}^{-1}$  and the surface conductivity was determined from the isoconductivity point (Shainberg and Levy, 1975). The bentonite data are from Lima et al. (2010). The data for illite is coming from Cremers et al. (1966). Note that for Na-bentonites the surface area can be as low as  $20\text{--}40 \text{ m}^2 \text{g}^{-1}$  according to Kaufhold et al. (2010).

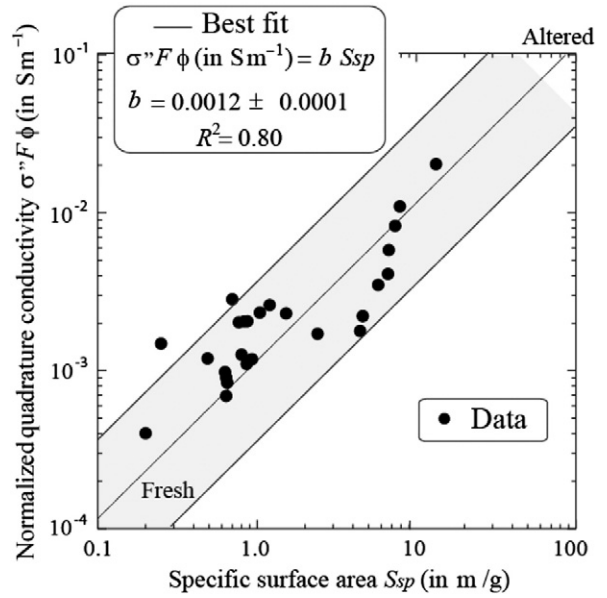


**Fig. 14.** Relationship between the normalized quadrature conductivity (product of the absolute value of the quadrature conductivity by the formation factor and the porosity) and the specific surface area measured with the BET method (expressed here in  $\text{m}^2 \text{g}^{-1}$ ) for the basaltic rocks from Hawaii. If we try to directly correlate the quadrature conductivity with the specific surface area data, the correlation coefficient is  $R^2 = 0.53$  instead of 0.80. The grey corresponds to the linear fit of the data with the 95% confidence interval.

4.5. Quadrature conductivity and normalized chargeability

In Fig. 14, we plot the normalized quadrature conductivity data (product of the absolute value of the quadrature conductivity by the formation factor and the porosity) versus the specific surface area measured with the BET method (expressed here in  $\text{m}^2 \text{g}^{-1}$ ). In Fig. 15, we plot the quadrature conductivity (absolute value) versus the specific

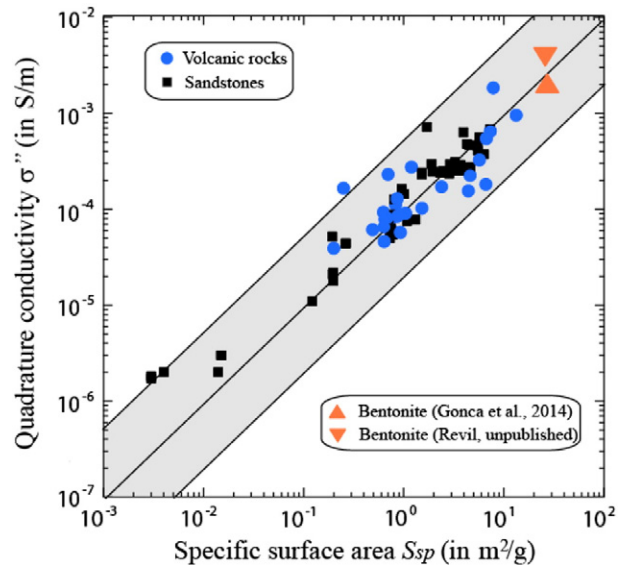


**Fig. 15.** Quadrature conductivity (absolute value) versus specific surface area and comparison between the data for the volcanic and sedimentary materials. The specific surface area is expressed in  $\text{m}^2 \text{g}^{-1}$  and measured with the BET nitrogen adsorption method. The bentonite sample is Sample B2 from Okay et al. (2014) ( $\sigma_w = 0.18 \text{ S m}^{-1}$ , 1 kHz). The sandstone data are from Table 2 of Niu et al. (2016b) with data from Weller et al. (2011), Niu et al. (2016a), Binley et al. (2005), Lesmes and Frye (2001), Börner (1992), Börner and Schön (1991) (quadrature conductivity at 1 Hz  $\sigma''$  and pore water conductivity NaCl close to  $0.1 \text{ S m}^{-1}$ ). The grey band corresponds to the linear trend predicted by the dynamic Stern layer model for the relationship between the two properties.

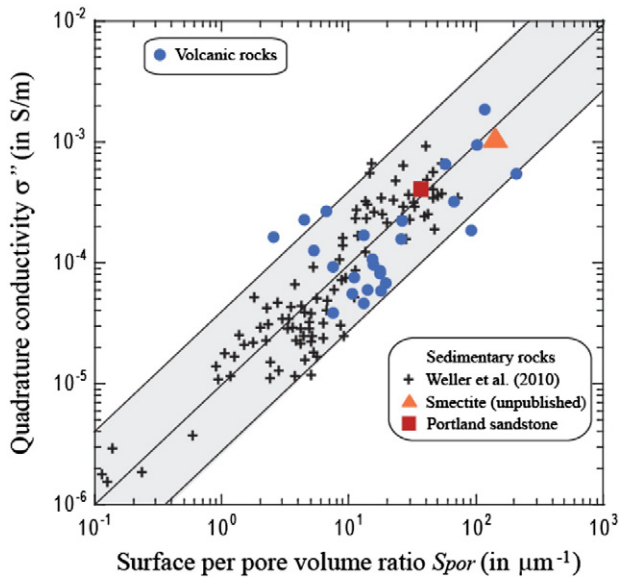


**Fig. 16.** Quadrature conductivity (absolute value) versus surface per pore volume ratio and comparison between the data for the volcanic and sedimentary materials. The paper by Weller et al. (2010) include data from Börner and Schön (1991), Scott (2003), Binley et al. (2005), Lesmes and Frye (2001), Kruschwitz (2008), Breede (2006), Schröder (2008), Slater and Glaser (2003), and Slater et al. (2006). The grey band corresponds to the linear trend predicted by the dynamic Stern layer model for the relationship between the two properties.

surface area measured with the BET nitrogen adsorption method. We also compare the data for the volcanic and sedimentary materials. For both Figs. 14 and 15, we see a high correlation between the quadrature conductivity and the specific surface area in agreement with the predictions by Eqs. (10) and (17).

In Figs. 16 and 17, we plot the quadrature conductivity and the normalized chargeability versus the surface per pore volume ratio. We see

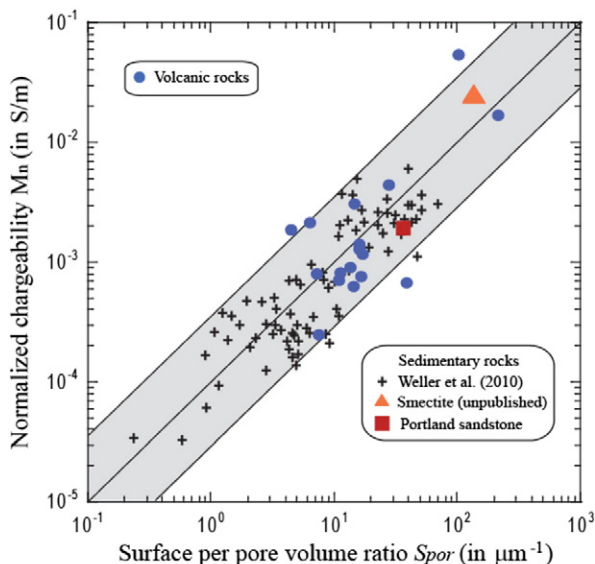


**Fig. 17.** Normalized chargeability versus surface per pore volume ratio and comparison between the data for the volcanic and sedimentary materials. The data for the Portland sandstone is from Niu et al. (2016a, 0.008 S m<sup>-1</sup> NaCl, 100 Hz close to the peak frequency). The paper by Weller et al. (2010) include data from Börner and Schön (1991), Scott (2003), Binley et al. (2005), Lesmes and Frye (2001), Kruschwitz (2008), Breede (2006), Schröder (2008), Slater and Glaser (2003), and Slater et al. (2006). The grey band corresponds to the linear trend predicted by the dynamic Stern layer model for the relationship between the two properties.

that these quantities are highly correlated as predicted by Eqs. (16) and (17). From Figs. 16 and 17, we see that the normalized chargeability is approximately ten times larger than the quadrature conductivity, which is consistent with  $\sigma'' \approx -M_n/\alpha$  with  $\alpha = 10$  as discussed in Section 4.2 and shown in Fig. 10.

## 5. Stern layer mobility and partition coefficient

Our last goal is to determine the mobility of the counterions in the Stern layer and the partition coefficient of the counterions between the Stern and diffuse layers using the trends shown in Figs. 13 to 17. Starting with the apparent mobility for surface conductivity  $B = \beta_{(+)}(1-f) + \beta_{(+)}^S f$  and Eq. (19), and after few algebraic manipulations, we obtain

$$f = 1 - \frac{B(1-R)}{\beta_{(+)}}. \quad (24)$$

Since we already determined the values of the three parameters entering this equation ( $B = 4.3 \times 10^{-9} \text{ m}^2 \text{ V}^{-1} \text{ s}^{-1}$ , see Section 4.3 above,  $R = 0.37$  (see Revil et al., 2015), and finally  $\beta_{(+)}(\text{Na}^+, 25^\circ \text{C}) = 5.2 \times 10^{-8} \text{ m}^2 \text{ s}^{-1} \text{ V}^{-1}$ , mobility of sodium in water), we obtain  $f = 0.95$ . In other words, 95% of the counterions are located or partitioned in the Stern layer. This is consistent with the values generally used in the dynamic Stern layer model (Revil, 2013).

We can also determine the value of the mobility of the cations in the Stern layer. Starting with the same equations, we obtain

$$\beta_{(+)}^S = \beta_{(+)} \frac{R(1-f)}{f(1-R)}. \quad (25)$$

Taking  $\beta_{(+)}(\text{Na}^+, 25^\circ \text{C}) = 5.2 \times 10^{-8} \text{ m}^2 \text{ s}^{-1} \text{ V}^{-1}$ ,  $R = 0.37$ , and  $f = 0.95$ , we obtain  $\beta_{(+)}^S = 1.6 \times 10^{-9} \text{ m}^2 \text{ s}^{-1} \text{ V}^{-1}$  and therefore a ratio  $\beta_{(+)} / \beta_{(+)}^S \approx 32$ . This is ten times higher than in our previous papers. The difference is explained by the fact that in our previous papers, we neglected the difference between quadrature conductivity and normalized chargeability and therefore we considered  $\alpha = 1$  while here we demonstrated that  $\alpha \approx 10$ . Low mobility in the Stern layer is partially supported by molecular dynamic simulations (e.g., Chang et al., 1995; Bourg and Sposito, 2010).

## 6. Conclusions

We have developed a database to study the relationship between induced polarization and alteration of volcanic rocks. The alteration is characterized here through specific surface area measurements obtained with the BET nitrogen adsorption method. We observe clear correlations between surface conductivity, normalized chargeability, and quadrature conductivity with the specific surface area. Follow up works will be focused on connecting induced polarization to the mechanical strength of volcanic rocks in the laboratory. In the field, our results implies that we can use spectral or time-domain induced polarization data to map in 3D alteration in volcanic edifices with application to geohazard.

## Acknowledgements

Funding for the drilling and initial characterization of the recovered rocks was provided primarily by the U.S. Army through the Pacific Cooperative Ecosystems Study Unit, with additional support from the National Science Foundation. We thank DOE (Geothermal Technology Advancement for Rapid Development of Resources in the U.S., GEODE, Award #DE-EE0005513) for funding. We warmly thank the two referees and the editor for their time and very positive comments regarding our manuscript.

## References

- Aizawa, K., Ogawa, Y., Ishido, T., 2009a. Groundwater flow and hydrothermal systems within volcanic edifices: delineation by electric self-potential and magnetotellurics. *J. Geophys. Res.* 114, B01208. <http://dx.doi.org/10.1029/2008JB005910>.
- Aizawa, K., Ogawa, Y., Mishina, M., Takahashi, K., Nagaoka, S., Takagi, N., Sakanaka, S., Miura, T., 2009b. Structural controls on the 1998 volcanic unrest at Iwate volcano: relationship between a shallow, electrically resistive body and the possible ascent route of magmatic fluid. *J. Volcanol. Geotherm. Res.* 187:131–139. <http://dx.doi.org/10.1016/j.jvolgeores.2009b.08.009>.
- Akayuli, C., Ofose, B., Nyako, S.O., Kwabena, O.O., 2013. The influence of observed clay content on shear strength and compressibility of residual sandy soils. *Int. J. Eng. Res. Appl.* 3 (4), 2538–2542.
- Archie, G.E., 1942. The electrical resistivity log as an aid in determining some reservoir characteristics. *Petroleum Trans. AIME* 146, 54–62.
- Bernabé, Y., Revil, A., 1995. Pore-scale heterogeneity, energy dissipation and the transport properties of rocks. *Geophys. Res. Lett.* 22 (12), 1529–1552.
- Bernard, M.-L., Zamora, M., Géraud, Y., Boudon, G., 2007. Transport properties of pyroclastic rocks from Montagne Pelée volcano (Martinique, Lesser Antilles). *J. Geophys. Res.* 112, B05205. <http://dx.doi.org/10.1029/2006JB004385>.
- Binley, A., Slater, L.D., Fukes, M., Cassiani, G., 2005. Relationship between spectral induced polarization and hydraulic properties of saturated and unsaturated sandstone. *Water Resour. Res.* 41 (12), W12417. <http://dx.doi.org/10.1029/2005WR004202>.
- Bleil, D.F., 1953. Induced polarization, a method of geophysical prospecting. *Geophysics* 18, 636–661.
- Börner, F.D., 1991. Untersuchungen Zur Komplexen Elektrischen Leitfähigkeit von Gesteinen im Frequenzbereich von 1 Millihertz Bis 10 Kiloherz. Unpublished Dissertation, Bergakademie Freiberg, Germany.
- Börner, F.D., 1992. Complex Conductivity Measurements of Reservoir Properties. Proceedings of the Third European Core Analysis Symposium, Paris pp. 359–386.
- Börner, F.D., Schön, J.H., 1991. A relation between the quadrature component of electrical conductivity and the specific surface area of sedimentary rocks. *Log. Anal.* 32, 612–613.
- Bourg, I., Sposito, G., 2010. Connecting the molecular scale to the continuum scale for diffusion processes in smectite-rich porous media. *Environ. Sci. Technol.* 44:2085–2091. <http://dx.doi.org/10.1021/es903645a>.
- Breede, K., 2006. SIP-Messungen an Sandsteinen. Diploma thesis, Technische Universität Clausthal, Germany.
- Brooks, B.A., Foster, J.H., Bevis, M., Frazer, L.N., Wolfe, C.J., Behn, M., 2006. Periodic slow earthquakes on the flank of Kilauea volcano, Hawaii. *Earth Planet. Sci. Lett.* 246, 207–216.
- Brunauer, S., Emmett, P.H., Teller, E., 1938. Adsorption of gases in multimolecular layers. *J. Am. Chem. Soc.* 60 (2):309–319. <http://dx.doi.org/10.1021/ja01269a023>.
- Chang, F.-R.C., Skipper, N.T., Sposito, G., 1995. Computer simulation of interlayer molecular structure in sodium montmorillonite hydrates. *Langmuir* 11, 2734–2741.
- Cianetti, S., Giunchi, C., Casarotti, E., 2012. Volcanic deformation and flank instability due to magmatic sources and frictional rheology: the case of Mount Etna. *Geophys. J. Int.* 191 (3):939–953. <http://dx.doi.org/10.1111/j.1365-246X.2012.05689.x>.
- Cremers, A., 1968. Surface conductivity in sodium clays. *Isr. J. Chem.* 6, 195–202.
- Cremers, A., Van Loon, J., Laudelout, H., 1966. Geometry effects for specific electrical conductance in clays and soils. In: Biley, S.W. (Ed.), *Clays and Clay Minerals*. Proceeding of the 14th National Conference, Berkeley, California. Pergamon Press, Oxford.
- Dakhnov, V.N., 1941. Electrical Well Logging, Interpretation of Electric Logs (Moscow).
- Frolova, J., Ladygin, V., Rychagov, S., Zukhubaya, D., 2014. Effects of hydrothermal alterations on physical and mechanical properties of rocks in the Kuril–Kamchatka island arc. *Eng. Geol.* 183, 80–95.
- Godelitsas, A., Gamaletos, P., Kotsis, M.R., 2010. Mordenite-bearing tuffs from Prassa quarry, Kimolos island, Greece. *Eur. J. Mineral.* 22 (6). <http://dx.doi.org/10.1127/0935-1221/2010/0022-2058>.
- Gonzales, K., Finizola, A., Lénat, J.F., Macedo, O., Ramos, D., Thouret, J.C., Fournier, N., Cruz, V., Pistre, K., 2014. Asymmetrical structure, hydrothermal system and edifice stability: the case of Ubinas volcano, Peru, revealed by geophysical surveys. *J. Volcanol. Geotherm. Res.* 276:132–144. <http://dx.doi.org/10.1016/j.jvolgeores.2014.02.020>.
- Iverson, R.M., 1995. Can magma-injection and groundwater forces cause massive landslides on Hawaiian volcanoes? *J. Volcanol. Geotherm. Res.* 66, 295–308.
- Kauahikaua, J., Hildenbrand, T., Webring, M., 2000. Deep magmatic structures of Hawaiian volcanoes, imaged by three-dimensional gravity models. *Geology* 28, 883–886.
- Kaufhold, S., Dohrmann, R., Klinkenberg, M., Siegesmund, S., Ufer, K., 2010. N<sub>2</sub>-BET specific surface area of bentonites. *J. Colloid Interface Sci.* 349, 275–282.
- Komori, S., Kagiya, T., Hoshizumi, H., Takakura, S., Mimura, M., 2010. Vertical mapping of hydrothermal fluids and alteration from bulk conductivity: simple interpretation on the USDP-1 site, Unzen Volcano, SW Japan. *J. Volcanol. Geotherm. Res.* 198 (3–4), 339–347.
- Kruschwitz, S., 2008. Assessment of the Complex Resistivity Behavior of Salt Affected Building Materials. Ph.D. Thesis. Federal Institute for Materials Research and Testing BAM, Germany.
- Kuila, U., 2007. Measurement and Interpretation of Porosity and Pore-size Distribution in Mudrocks: The Whole Story of Shales. Ph.D. thesis. Colorado School of Mines.
- Lesmes, D.P., Frye, K.M., 2001. Influence of pore fluid chemistry on the complex conductivity and induced polarization responses of Berea sandstone. *J. Geophys. Res.* 106 (B3), 4079–4090.
- Lima, A.T., Loch, J.P.G., Kleingeld, P.J., 2010. Bentonite electrical conductivity: a model based on series-parallel transport. *J. Appl. Electrochem.* 40:1061–1068. <http://dx.doi.org/10.1007/s10800-009-0060-7>.
- Lira, B.P., Polo, A.O., Sánchez, E.M.O., Ruiz, E.R., Sandoval, O.A.A., García, F.P., Ramírez, C.A.G., 2013. Physical characterization of an extensive volcanic rock in México: “red tezontle” from Cerro de la Cruz, in Tlahuelilpan, Hidalgo. *Acta Universitaria* 23 (4), 9–15.
- Lowell, S., Shields, J.E., 1979. Powder Surface Area and Porosity. 2nd ed. Chapman and Hall, 234, p. 1.
- Lyklema, J., Dukhin, S., Shilov, V., 1983. The relaxation of the double layer around colloidal particles and the low-frequency dielectric dispersion. Part I: theoretical considerations. *J. Electroanal. Chem. Interfacial Electrochem.* 143:1–21. [http://dx.doi.org/10.1016/S0022-0728\(83\)80251-4](http://dx.doi.org/10.1016/S0022-0728(83)80251-4).
- Masson, D.G., Watts, A.B., Gee, M.J.R., Urgeles, R., Mitchell, N.C., Le Bas, T.P., Canals, M., 2002. Slope failures on the flanks of the western Canary Islands. *Earth Sci. Rev.* 57, 1–35.
- Mejus, L., 2014. Using Multiple Geophysical Techniques for Improved Assessment of Aquifer Vulnerability. Ph.D. thesis. Lancaster University.
- Meller, C., Kohl, T., 2014. The significance of hydrothermal alteration zones for the mechanical behavior of a geothermal reservoir. *Geothermal Energy* 2 (12), 21.
- Moore, J.G., Clague, D.A., Holcomb, R.T., Lipman, P.W., Normark, W.R., Torresan, M.E., 1989. Prodigious submarine landslides on the Hawaiian Ridge. *J. Geophys. Res.* 94, 17,465–17,484.
- Nielsen, M.E., Fisk, M.R., 2008. Data report: specific surface area and physical properties of subsurface basalt samples from the east flank of Juan de Fuca Ridge and the Expedition 301 Scientists. In: Fisher, A.T., Urabe, T., Klaus, A. (Eds.), *Proc. IODP, 301, College Station, TX*. (Integrated Ocean Drilling Program Management International, Inc.) <http://dx.doi.org/10.2204/iodp.proc.301.205>.
- Niu, Q., Prasad, M., Revil, A., Saidian, M., 2016b. Textural control on the quadrature conductivity of porous media. *Geophysics* 81 (5):E297–E309. <http://dx.doi.org/10.1190/GEO2015-0715.1>.
- Niu, Q., Revil, A., Saidian, M., 2016a. Salinity influence of the complex surface conductivity of Portland sandstone. *Geophysics* 81 (2):D125–D140. <http://dx.doi.org/10.1190/GEO2015-0426.1>.
- Okay, G., Leroy, P., Ghorbani, A., Cosenza, P., Camerlynck, C., Cabrera, J., Florsch, N., Revil, A., 2014. Spectral induced polarization of clay-sand mixtures. Experiments and modelling. *Geophysics* 79 (6):E353–E375. <http://dx.doi.org/10.1190/GEO2013-0347.1>.
- Phillips, K.A., Chadwell, C.D., Hildebrand, J.A., 2008. Vertical deformation measurements on the submerged south flank of Kilauea volcano, Hawai'i reveal seafloor motion associated with volcanic collapse. *J. Geophys. Res.* 113, B05106. <http://dx.doi.org/10.1029/2007JB005124>.
- Reid, M.E., 2004. Massive collapse of volcano edifices triggered by hydrothermal pressurization. *Geology* 32:373–376. <http://dx.doi.org/10.1130/G20300.1>.
- Revil, A., 2012. Spectral induced polarization of shaly sands: influence of the electrical double layer. *Water Resour. Res.* 48, W02517. <http://dx.doi.org/10.1029/2011WR011260>.
- Revil, A., 2013. Effective conductivity and permittivity of unsaturated porous materials in the frequency range 1 MHz–1 GHz. *Water Resour. Res.* 49:306–327. <http://dx.doi.org/10.1029/2012WR012700>.
- Revil, A., Binley, A., Mejus, L., Kessouri, P., 2015. Predicting permeability from the characteristic relaxation time and intrinsic formation factor of complex conductivity spectra. *Water Resour. Res.* 51. <http://dx.doi.org/10.1002/2015WR017074>.
- Revil, A., Cathles, L.M., Shosa, J., Pezard, P.A., de Larouziere, F.D., 1998. Capillary sealing in sedimentary basins: a clear field example. *Geophys. Res. Lett.* 25 (3), 389–392.
- Revil, A., Eppheimer, J.D., Skold, M., Karaoulis, M., Godinez, L., Prasad, M., 2013. Low-frequency complex conductivity of sandy and clayey materials. *J. Colloid Interface Sci.* 398, 193–209.
- Revil, A., Hermitte, D., Spangenberg, E., Cochémé, J.J., 2002. Electrical properties of zeolitized volcanoclastic materials. *J. Geophys. Res.* 107 (B8):2168. <http://dx.doi.org/10.1029/2001JB000599>.
- Revil, A., Kessouri, P., Torres-Verdin, C., 2014. Electrical conductivity, induced polarization, and permeability of the Fontainebleau sandstone. *Geophysics* 79 (5):D301–D318. <http://dx.doi.org/10.1190/GEO2014-0036.1>.
- Ridge, M., 1983. A combustion method for measuring cation exchange capacity of clay minerals. *Log. Anal.* 24 (3), 4–11.
- Ruffet, C., Gueguen, Y., Darot, M., 1991. Complex conductivity measurements and fractal nature of porosity. *Geophysics* 56 (6), 758–768.
- Schlumberger, C., 1920. Study of Underground Electrical Prospecting. Paris, p. 99.
- Schröder, H., 2008. SIP-Messungen an Mit Unterschiedlichen Salzlösungen Gesättigten Sandsteinen: Diploma Thesis. Technische Universität Clausthal, Germany.
- Schuffe, J.A., 1959. Cation exchange and induced polarization. *Geophysics* 24 (1), 164–166.
- Scott, J.B.T., 2003. Low-frequency Electrical Spectroscopy of Sandstone. Ph.D. thesis. University of Birmingham.
- Scott, J.B.T., 2006. The origin of the observed low-frequency electrical polarization in sandstones. *Geophysics* 71 (5):G235–G238. <http://dx.doi.org/10.1190/1.2258092>.
- Seigel, H.O., 1959. Mathematical formulation and type curves for induced polarization. *Geophysics* 24, 547–565.
- Sen, P.N., Straley, C., Kenyon, W.E., Whittingham, M.S., 1990. Surface-to-volume ratio, charge density, nuclear magnetic relaxation, and permeability in clay-bearing sandstones. *Geophysics* 55 (1), 61–69.
- Shainberg, I., Levy, R., 1975. Electrical conductivity of Na-montmorillonite clay suspensions. *Clay Clay Miner.* 23 (205), 210.
- Shinzato, M.C., Montanheiro, T.J., Janasi, V.A., Andrade, S., Yamamoto, J.K., 2012. Removal of Pb<sup>2+</sup> from aqueous solutions using two Brazilian rocks containing zeolites. *Environ. Earth Sci.* 66:363–370. <http://dx.doi.org/10.1007/s12665-011-1245-z>.
- Shuey, R.T., Johnson, M., 1973. On the phenomenology of electrical relaxation in rocks. *Geophysics* 38:37–48. <http://dx.doi.org/10.1190/1.1440331>.

- Siniscalchi, A., Tripaldi, S., Neri, M., Balasco, M., Romano, G., Ruch, J., Schiavone, D., 2012. Flank instability structure of Mt. Etna inferred by a magnetotelluric survey. *J. Geophys. Res.* 117, B03216. <http://dx.doi.org/10.1029/2011JB008657>.
- Slater, L.D., Glaser, D.R., 2003. Controls on induced polarization in sandy unconsolidated sediments and application to aquifer characterization. *Geophysics* 68, 1547–1558.
- Slater, L.D., Ntarlagiannis, D., Wishart, D., 2006. On the relationship between induced polarization and surface area in metal-sand and clay-sand mixtures. *Geophysics* 71 (2), A1–A5.
- Tarasov, K., Titov, K., 2013. On the use of the Cole–Cole equations in spectral induced polarization. *Geophys. J. Int.* 195, 352–356.
- Thommes, M., Cychoz, K.A., 2014. Physical adsorption characterization of nanoporous materials: progress and challenges. *Adsorption* 20 (2–3), 233–250.
- Urgeles, R., Masson, D.G., Canals, M., Watts, A.B., Le Bas, T., 1999. Recurrent large-scale landsliding on the west flank of La Palma, Canary Islands. *J. Geophys. Res.* 104, 25,331–25,348.
- Usui, Y., Ogawa, Y., Aizawa, K., Hashimoto, T., Koyama, T., Kagiyama, T., 2016. Three-dimensional resistivity structure of Asama Volcano revealed by data-space magnetotelluric inversion using unstructured tetrahedral elements. *Geophys. J. Int.* 208 (3):1359–1372. <http://dx.doi.org/10.1093/gji/ggw459>.
- Vacquier, V., Holmes, C.R., Kintzinger, P.R., LaVergne, M., 1957. Prospecting for ground water by induced electrical polarization. *Geophysics* 22, 660–687.
- Van Voorhis, G.D., Nelson, P.H., Drake, T.L., 1973. Complex resistivity spectra of porphyry copper mineralization. *Geophysics* 38 (1):49–60. <http://dx.doi.org/10.1190/1.1440333>.
- Vinegar, H.J., Waxman, M.H., 1984. Induced polarization of shaly sands. *Geophysics* 49: 1267–1287. <http://dx.doi.org/10.1190/1.1441755>.
- Waxman, M.H., Smits, L.J.M., 1968. Electrical conductivities in oil bearing shaly sands. *Soc. Pet. Eng. J.* 243, 107–122.
- Weller, A., Breede, K., Slater, L., Nordsiek, S., 2011. Effect of changing water salinity on complex conductivity spectra of sandstones. *Geophysics* 76 (5):F315–F327. <http://dx.doi.org/10.1190/geo2011-0072.1>.
- Weller, A., Slater, L., Nordsiek, S., Ntarlagiannis, D., 2010. On the estimation of specific surface per unit pore volume from induced polarization: a robust empirical relation fits multiple data sets. *Geophysics* 75 (4):WA105–WA112. <http://dx.doi.org/10.1190/1.3471577>.
- Yukselen, Y., Kaya, A., 2008. Suitability of the methylene blue test for surface area, cation exchange capacity and swell potential determination of clayey soils. *Eng. Geol.* 102: 38–45. <http://dx.doi.org/10.1016/j.enggeo.2008.07.002>.
- Zimmermann, E., Kemna, A., Berwix, J., Glaas, W., Munch, H., Huisman, J., 2008. A high-accuracy impedance spectrometer for measuring sediments with low polarizability. *Meas. Sci. Technol.* 19 (10), 105603.